Nanoscale

Accepted Manuscript

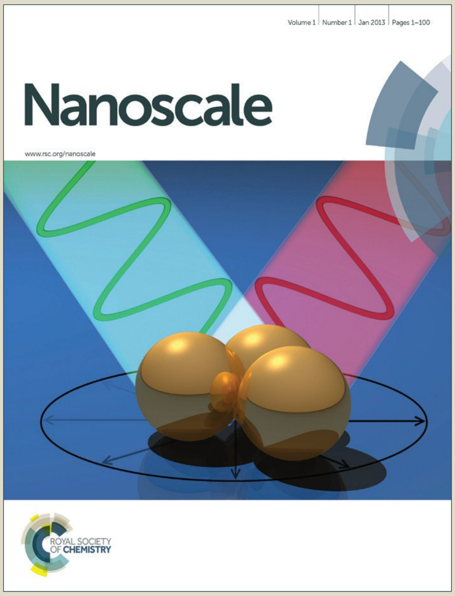

ROYAL SOCIETY OF CHEMISTRY

www.rsc.org/nanoscale

Journal Name

ARTICLE

Plasma-Assisted Synthesis and Pressure-Induced Structural Transition of Single-Crystalline SnSeNanosheets

Received 00th January 20xx,
Accepted 00th January 20xx

DOI: 10.1039/x0xx00000x

www.rsc.org/

Jianzhang,[a] HongyangZhu,[a] XiaoxinWu,[a] Hang Cui,[c] DongmeiLi,[a] JunruJiang,[a] ChunxiaoGao,[a] Qiushi Wang[*b] and Qiliang Cui[*a]

Two-dimensional tin selenide (SnSe) nanosheets were synthesized using a plasma assisted direct current arc discharge method. The structural characterization indicates that the nanosheet is single-crystalline with the average thickness of ~25 nm while the lateral dimension of ~500 nm. The high pressure behaviors of as-synthesized SnSe nanosheets were investigated by in situ high-pressure synchrotron angle-dispersive X-ray diffraction and Raman scattering up to ~30 GPa in diamond anvil cells at room temperature. A second-order isostructural continuous phase transition (Pnma→Cmcm) was observed at ~7 GPa, which is much lower than the transition pressure of bulk SnSe. The reduction of transition pressure is induced by the volumetric expansion with softening of Poisson ratio and shear modulus. Meanwhile, the measured zero-pressure bulk modulus of SnSe nanosheets coincides with the bulk SnSe. This abnormal phenomenon is attributed to the unique intrinsic geometry in nanosheets. The high-pressure bulk modulus is much higher than theoretical value. The pressure-induced morphology change should be responsible for the improved bulk modulus.

Introduction

The past decades have witnessed greatprogress in producing the ultrathin nanomaterials.[1-5]Since the first introduction of the strictly two-dimensional(2D) atomic crystal graphene,[6] 2D nanomaterial is becoming a highly promising new class of materials and has sparkeda diversity of applicationin the next generation of electronic and optoelectronic devicesdue to their unique dimension-dependent optical,[7-9] electrical,[10,11] magnetic[12,13] and superconducting properties.[14,15]As a typical2D layered material, tin selenide (SnSe) nanocrystals have been exploited in a diverse range of fields such as solar energy conversion,[16,17]holographic recording,[18] near-infrared optoelectronic devices[19] and rechargeable Li ion batteries.[20]In addition, other advantages, suchas earth-abundance, less toxicity and chemical stability, have also made the controlled synthesis and property study of SnSe afocus of interest.

Current synthetic strategies for SnSe nanostructure primarily focus on the so-called wet-chemical synthetic processes, such as solvothermal, chemicalbath deposition and electrodeposition. Various nanostructures, such as 0D nanocrystals,[21,22] 1D nanowires[17,23]and 2D nanosheets,[24,25] have been prepared through these methods. However, the precursor, intermediate and solvent residues adsorbed at the surface of products are difficult to remove and substantially modify the intrinsic properties. Meanwhile,“solvent-free” synthesis approaches (*e.g.*chemical or physical vapor depositions (CVD/PVD))[26-28] have also been explored for the growth of SnSe. These methods are easy operation, reaction hypotoxicity, assemble fewer defects and avoid residual impurities. However, the synthesis process normallyneeds complex procedures, essential substrates and long reaction times, which would reduce the synthetic efficiency. Thus, controlled synthesis of pure-phase and free-standing SnSe nanostructure in a convenient way is still a great challenge. One aimof this work is to explore a rapid, low-cost and high-yield method for synthesis SnSenanosheets (NSs).

In general, the properties of nanomaterials largely depend on its crystal phase, surface area, morphology and architecture. Therefore, structural stability of sheet-shape nanomaterials is one of the crucial factors for their application. It is well known that high pressure provides a powerful method for researching the physicochemicalproperties and structural phase transitions of materials. Most previous researches on SnSe mainly focus on the synthesis method and property analysis. Only a fewstudies on high-pressure behavior of SnSe have been reported. In 1984, Chattopadhyay*et al.* reported that SnSe does not undergo any phase transition up to 34 GPa by energy dispersive X-ray diffraction study.[29] In 1990, Peters *et al.* investigated the crystal structure of SnSe under low-pressure range using Mössbauer spectroscopy. They found that the identified change of interlayer bonds driven SnSe from a predominantly 2D to a more 3D material below 3 GPa.[30] After that, Carlone*et al.*[31] measured the optical gaps of SnSe up to 4 GPa and Agarwal*et al.*[32] investigated the electrical resistivity and thermopower around 6 GPa. In all these early works, although some subtle changes have been observed under high pressure, the exact origin of these changes was still unclear and no phase transition has

---

[a] State Key Laboratory of Superhard Materials, Jilin University, Changchun 130012, Jilin, China.E-mail: cql@jlu.edu.cn
[b] College of New Energy, Bohai University, JinZhou 121013, Liaoning, China.E-mail: wang_jiu_jiu@foxmail.com
[c] College of Physics, Jilin University, Changchun 130012, Jilin, China

† Electronic Supplementary Information (ESI) available. See: DOI: 10.1039/x0xx00000x

been found. More recently, Loa *et al.* observed that SnSe undergoes a continuous transition from the GeS-type to TII-type structure with a transition pressure (P_{T}) of 10.5 GPa based on the synchrotron radiation technology.[33] This phase transition sequence is closely related to the recent computational works on GeS,[34] GeSe,[35] SnS[36] and SnSe[37] itself. Typically, in 2011, Alptekin*et al.* put forward that SnSe undergoes a second-order phase transition from orthorhombic (*Pnma*) structure to orthorhombic (*Cmcm*) structure at 7 GPa, using *ab initio* constant-pressure method. It should be noted that the P_{T} is significantly less than the experimental results and the high-pressure bulk modulus (B_0) is not mentioned in the experiment. In order to clarify the uncertainties, reliable and detailed high-pressure experiments is highly anticipated. In addition, previous studies on nanomaterials under high pressure have revealed a series of interesting phenomena and novel properties, which is different from their corresponding micro and bulk counterparts. However, to our knowledge, there has been no report of high pressure study on nano-scaled SnSe.

Herein, a novel, efficient and simple method is reported forthe synthesis ofSnSe NSs, in which tin (Sn) and selenium (Se) metal powders served as the precursor is essential for avoiding the introduction of impurities.Furthermore, in order to explore the structural stabilities and vibrational properties under high pressure, the obtained SnSeNSs have been investigated by*in situ* synchrotron angle-dispersive X-ray diffraction (ADXRD)and Raman scattering techniques.Compared with bulk SnSe, certain unusual pressureresponses have been observed. The factorscontribute to these distinct high-pressure behaviors are reported and discussed in this paper.These phenomenawill help us to further investigate the undisclosed intrinsic physical properties of SnSe NSs. We expect that this work not only provide valuable high-pressure experimental information of SnSe, but also offer the opportunity for better understand the pressure-induced phase transition behaviors of other IV-VI layered compounds at nano-scale.

Experimental

Synthesis of SnSe NSs.

The synthesis was carried out in an improved direct current(DC)arc discharge plasma setup.[38]Schematic diagram of the experimental set-up is shown in Fig. S1. A tungsten rod (purity: 99.99%) with 5 mm in diameter and 30 cm in lengthwas used as the cathode. Sn and Se powders (purity: 99.99%) were mixed with a molar ratio 1:1 and then pressed into ingot.The ingotwas place on the graphite groove as the anode.The reaction chamber was first evacuated to less than 1 Pa and then filled with argon. This cycle was repeatedseveral times to remove the residual air completely, andthen working gas (Ar, purity: 99.999%) was introduced into the chamber. The Ar pressure isselected at 10kPa. When the DC arc discharge was ignited, the input current was maintained at 100A and thevoltage was a little higher than 15 V.The dischargingprocess was maintained for 5 min.After that, the productswere passivated for 6 hours in pure Ar gas at 80 kPa. Finally, the high-yield fluffy dark gray samples were collected at the surface of the water-cooling wall.

Characterization.

Powder X-ray diffractometry (XRD)data were collected on a Rigaku D/max γAdiffractometerworking with a using Cu-Kα target (λ = 0.154178 nm). Scanning electron microscopy (SEM) images were obtained *via* a FEI MAGELLAN-400 microscope.High-resolution transmission electron microscopy (HRTEM) images, energy-dispersive X-ray spectroscopy (EDS), STEM-EDS elementalmaps (Mapping) and selected area electron diffraction (SAED) patterns were taken on a JEM-2200FS transmission electron microscopeusing an accelerating voltage of 200 kV.UV-vis diffuse reflectance spectrum (DRS) was monitored by aShimadzu UV-3150 spectrometer.

High-pressure studies.

In situ high-pressure synchrotron ADXRD measurements were performed at the 4W2 beamline of the Beijing Synchrotron Radiation Facility (BSRF) with the beam wavelengthof 0.6199 Å.A Mao-Bell-type diamondanvil cell (DAC) with culet diameter of 400 μmwas used to preindent the T-301 stainless steel gasket to 60 μmthickness.A 100-μm-diameter hole was drilled at the center of the gasket to form the sample chamber.The sample with a tiny ruby chip was loaded into the sample chamber with a quasi-hydrostaticpressure medium (methanol : ethanol = 4:1).The pressure was determined from thefrequency shift of the ruby R1 fluorescence line.[39] The Bragg diffraction rings were recorded with a MAR345 CCD detector and the average acquisition time was 500 s. The XRD diffraction patterns were integrated fromthe images with FIT2D software andwere refined using Rietveld method with Material Studio software. High-pressure Raman measurements were performed at room temperature using a solid-state diode-pumped Nd:Vanadate laser (Coherent Inc.) with 532 nm wavelength as excitation source. An Acton SpectraPro 500i spectrometer with 1800 gr/mm holographic grating and a liquid-nitrogen-cooled CCD detector (Princeton Instruments, 1340*100) were used. The laser power focused on the sample was operatedat 3 mw (after filer) to avoid heating effect.

Results and discussion

Fig. 1a shows a typical low-magnification SEM image of as-synthesized SnSe NSs, displaying most of which exhibituniform sheet-like morphology.Fig. 1b and 1c are higher-magnification SEM images of SnSe NSs.It is apparent that the products have the characteristics of ultra-thin, rhombus-shaped and smooth surface.The thickness of SnSe NS is ~25 nm while the lateral dimension reaches ~500 nm. Powder XRD was performed toanalyze the phase and crystallinity of SnSe NSs. As shown inFig. 1d, all diffractionpeaks were indexed to the orthorhombicGeS-type SnSe crystal structure(JCPDS No.32-1382, *Pnma*) with the lattice parameter of a = 11.579(5) Å, b = 4.185(2) Å and c = 4.427(2) Å. No additional crystalline impurityphases are observed.The corresponding unit cell volume (V_0=214.52 Å^3) is 0.5% larger than that of bulk SnSe (V_0=213.41 Å^3).

In order to further elucidate the nanostructure of SnSe NSs, TEM and HRTEM investigation were performed and shown in Fig. 2. The typical morphology of a single NS is shown in Fig. 2b and its corner angle was measured as ~86°. The single-crystalline feature was verified by HRTEM. As shown in Fig. 2c, two apparent planes revealing the lattice spacing at ~0.30 nm and the intersection angle of ~86° as well. The SAED pattern (inset in Fig. 2c) indicates the NS is bounded by {011} planes and orientated with the exposed plane along [100] plane direction. To identify the element distribution and Sn/Se atom ratio, Mapping and EDS analysis were recorded (Fig. 2d). The results reveal that the two elements are distributed homogeneously in each NS and exhibit no apparent element separation or aggregation. The atom ratio of Sn/Se is nearly 1:1 (exact value is 49.49 : 50.51), which is well consistent with the stoichiometric feature of SnSe.

As mentioned above, the corner angle of NSs exactly matches the intersection angle of {011} planes. Thus, the growth mechanism of SnSe NSs should be related to the crystal structure itself. It is well-known that SnSe adopts a layered crystal structure with atoms arranged resembling distortedNaCl structure.[25] Similar to other group IV-VI binary materials such as SnS, GeS, and GeSe, the strong covalent bonds are present within atomic layers, which comprises zig-zag double layer planes of the tin and selenium atoms and is separated by a weak van der Waals force between the layers along the a-axis direction. Benefiting from the anisotropic atomic bonding nature, the growth rate will be much faster in b- and c-axis orientations compared to the a-axis, which will prefer to the formation of sheet-like morphology. This type of growth mechanism correspond with the previous growth model ofSnSe NSs which were synthesized on different substrates *via* a non-catalytic vapor phase synthesis method.[28]

Fig. S2 shows the UV–vis DRS of SnSe NSs. To determinethe indirect and direct optical bandgap values,Kubelka-Munk transformationswere performedby the following equations:[40]

$$A = -\lg (R) \qquad (1)$$

$$\mathrm{F}(R) = (1-R)^2/2R \qquad (2)$$

where A is absorbance, R is reflectance and F(R) is Kubelka–Munk. In the actual experiment, the relational expression becomes: $[\mathrm{F}(R)h\nu]^{1/n} = \mathrm{A}(h\nu - \mathrm{E_g})$. The value of n is 1/2 and 2 correspond to the direct and indirect transition, respectively. As shown in Fig. S2a, the onset of absorption was found to be in the near-infrared region at ~1400 nm. A plot of$[\mathrm{F}(R)h\nu]^2$ versus energy indicates a direct band gap of~1.18 eV (Fig. S2b), and a plot of $[\mathrm{F}(R)h\nu]^{1/2}$ versusenergy indicates an indirect band gap of ~0.92 eV(Fig. S2c). These values are consistent withprevious reports and meet the optimum band gap (Eg = 1.0~1.5 eV) of high-performance light absorbing materials.[41] It means that the as-synthesized SnSe NSs are appropriate for potential applications in solar cells,[16,21] radiation detectors[42] and memory switching devices.[43]

High-Pressure Synchrotron ADXRD Investigation.

It is well-known that high pressure is an effective approach to studythe structural stability and possible phasetransitions of bulk/nano-materials. The as-synthesized SnSe NSs are investigated by *in situ* high-pressure synchrotron ADXRD for furtherexploration. Representativehigh-pressure XRD patterns are shown in Fig. 3a and the pressure dependence *d*-spacing of the lattice planes are shown in Fig. 3b.During the entire compression processes, all diffraction peaks shift to higher angles with increasing pressure. Although noextra peaks appear in the XRD patterns, some inconspicuous variations such as shift rate and relative intensity of specificpeaks have been observed from 6.7 GPa to 14.3 GPa. From 6.7 GPa, the peaks of (002) and (312) planes gradually approachtheir adjacentpeaks of (020) and (420)planes (marked with hollow diamonds and right arrows), respectively, and completely mergewith them at 14.3 GPawith compression (marked with solid diamonds). The merged peaks move to the higher degrees up to the highest pressure we measure.Meanwhile, the intensity of peaks of (201) and (011) planes (marked with asterisksand down arrows) weakenedsignificantly and disappear at this pressure range. It could be concluded from above evidences that the initial phase translate into ahigher-symmetry isomorphic structure started at 6.7 GPa and completed at 14.3 GPa. This transition could also be observed more directly through the changing slope of the pressure dependence*d*-spacing in Fig. 3b. In order to confirm this conclusion, the Rietveld refinement of the patterns at 1.2GPa and 19.6GPa are carried out. As shown in Fig. 4, the initial and high-pressure phase exactly match the orthorhombic structurewith the space groupof *Pnma*(62) and *Cmcm* (63), respectively. And this phase transition sequence is consistent with the previousexperimental[33] and theoretical[37] studies on bulk SnSe.

In order to get more information about the structural stability,the axial compressibility of SnSe NSs have been investigated from the pressure dependence of the lattice parameters. As shown in Fig. 5a, the short *b*- and *c*-axis form anintersection at ~7 GPa, which indicate that the lattice parameters changed from $a>c>b$ to $a>b>c$ beyond this pressure. This change coincides with the previous studies on temperature-induced second-order structuraltransformation of SnSe.[29,44]The transition pressure (P_T) is consist with the ADXRD results as well. By taking a closer look at the relative lattice parameters (Fig. 5b), we observe a strong anisotropic compression. The*c*-axis is found to be more compressible than the other axes,although the *a*-direction is perpendicular to the layers which are pile up with a weak van der Walls coupling. Meanwhile, we observed some interesting changes in the pressure dependence of both a/c, a/b and c/b in the range of 7~14 GPa (Fig. 5c). More precisely, the initially “softest” *c*-axis reaches the *a*-axis in terms ofcompressibility above 7GPa, and the *b*-axis is becoming “stiffer”. Similar behavior was detected in the isostructuralGeSand GeSe using *ab initio* technique.[34,35]In which, the compression mechanism was described as follows. When the structure is subjected to pressure, the strongestcompression along the *c*-axis causes a significant reduction of the distance between the next nearest neighbor atoms. As a result, two new chemical bonds ofhigh-pressure phase are formed at a certain distance. This transformation mechanism also applies to the high pressure behavior of SnSe NSs. In addition, we display the P-V data of SnSe in Fig. 5d. The volume decreases monotonicallywithout any discontinuities.Thedata are divided into two groups (0~6.7 GPa and 14.3~29.2 GPa) and fitted with the Birch–Murnaghan(BM) equation of state (EOS):[45]

$$P = 3/2B_0[(V_0/V)^{7/3} - (V_0/V)^{5/3}]\{1 + 3/4(B_0' - 4) \times [(V_0/V)^{2/3} - 1]\} \qquad (3)$$

where $B_0$is the bulk modulus and B_0’is the pressure derivative.V and V_0 is the volume at pressure P and at ambient pressure, respectively.

The *Pnma* phase gives the bulk modulus B_0= 34.4(21)GPa with a fixed B_0'=4. This result is well consistent withtheoretical value 33.3 GPa[37] and experimental value 31.1 GPa.[33]The bulk modulus of the *Cmcm* phase is B_0 = 80.1(11)GPa with B_0' at 4, which exhibits a significantreduced compressibilitycompared to theoretical value (B_0 = 40.9GPa).[37]

When the pressure released to the ambient pressure, all diffraction peaks recovered to the shape of the initial structure, indicating the pressure-induced structural transformation is reversible. Thesedistinctive compressibility changes of specific structuralparameters are reminiscent of second-order isostructuraltransitions observed in related layered materials,[46,47]*i.e.*,structural transitions without any syngonychange and volumediscontinuities. Thus, we attribute the changed compressibility in SnSe above ~7GPa to asecond-order isostructural continuous phase transition.

Discussion

We should note that the P_T of SnSe NSs (~7 GPa) is much lower than that of bulk SnSe (~10.5 GPa). However, numerous studies on nanomaterials indicate that the reduction of particle size could lead to an apparent elevation of P_T.[48,49]Because the large pressure gradient can result in a significant decrease of P_T, the effect of the pressure-induced non-hydrostaticity in the sample chamber could be a possible reason. In this study, hydrostatic stress is achieved by immersing the sample in a pressurized fluid medium (M:E=4:1). This type of medium is able to maintain a hydrostatic/quasi-hydrostatic state up to 15 GPa. Because the observed P_T is located within the pressure range, it is thus believed that such a reduced P_T is not caused by the large pressure gradient across the sample. Moreover, a critical size of 15 nm has been uncovered for a large number of nanocrystalline materials.[50-52] Below 15 nm, nanomaterials display a unit cell volumetric expansion together with softening of the Poisson ratio and shear modulus, which would result in a reduction of P_T.[53] Interestingly, a volumetric expansion was observed at ambient pressure in SnSe NSs despite the size of NS is larger than the critical size. Hence, we have reason to believe that the abnormal volumetric expansion with the softening of Poisson ratio and shear modulus may also play a crucial role in the reduction of the P_T for this second-order isostructural continuous phase transition in SnSe NSs. In addition, the complete phase transition pressure (P_C) is quite sluggish and the phase transition pressure range was extended greatly. The sluggishness can be explained as a high-energy hindrance that prevents the rapid transition to high-pressure phase in nanomaterials.[54,55]

In general, for nanocrystalline materials, the bulk modulus elevate apparently as compared with their bulk materials by a higher surface energy contribution.[54,56] However, we note that the initial phase B_0 of SnSe NSs is consistent with the bulk SnSe. This distinct compressibility should be attributed to the unique intrinsic geometry of NSs. It can be explained as follows. The thickness of SnSe NS has an average size of ~25 nm and the lateral dimension reach an average length of ~500 nm. The size characteristics is considerably different from the conventional 1D nanowires and 0D nanoparticles, because even the lowest dimension is markedly larger than the critical particle size. Therefore, in terms of the size, the SnSe NS should be regarded as the corresponding bulk SnSe and exhibits the nature of bulk materials. Meanwhile, the high-pressure phase B_0 is much higher than theoretical value. We suggested that the pressure-induced morphology changes play an important role in the structural stability. For SnSe NSs, the fracture occurs more easily in this type of large-scale NSs under high pressure, especially during a structural transition. The zig-zag atomic arrangement in intralayer of SnSe was seriously distorted like a retractable spring or an accordion. The sheet-like morphology was serious damaged and the large-scaled NS were crushed to pieces with smaller size. This phenomenon of the pressure-induced morphological change has also been reported in CdSe[57]and ZnS[58] spherical nanocrystals. In order to confirm this assumption, TEM and HRTEM investigations of the quenchedsample have been performed. As shown in Fig. S3, the sample has been transformed into an irregular polymer composed of fragments. The lattice spacing of ~0.30 nm indicates that these fragments still have a crystalline nature, and the average particle size was reduced to ~10 nm. These fragments will show a higher surface energy than initial NSs and bulk materials, which will result in an enhancement of the bulk modulus.[59]The same results occurs in other sheet-like nanostructures such as CdSe[60,61] and Bi_2Te_3.[62]Therefore, we come to the conclusion that the pressure-induced morphology change should be responsible for the improved bulk modulus of high-pressure phase SnSe.

High-Pressure Raman Investigation.

In order to detect the pressure-inducedisostructural transitions, we performed the high-pressure Raman investigations up to 29.2 GPa at room-temperature. The starting SnSe has an orthorhombic structure *Pnma* (D_{2h}^{16}) space group withthe Sn and Seatoms in 4c Wyckoff positions (x, 1/4, z). The group-theoretical analysis indicates the following 12 modes are Ramanactive among 21 zone-center (Γ-point) phonon modes in the SnSe:[63]

$$\square\Gamma = 4A_g + 2B_{1g} + 4B_{2g} + 2B_{3g} \qquad (4)$$

The selected Raman scattering patterns of SnSe NSs at variouspressures are shown in Fig. 6a. Only five modes (3A_g at 75, 126, 162 cm^{-1},B_{1g} at 135 cm^{-1} and B_{3g} at 105 cm^{-1}) are detected atambient conditions, and the remaining modes are expected at low frequency rangeor have a low intensity. With the pressure increasing, A_g(2) mode merges with its neighboring B_{3g}mode and cannot be resolved above 6.8GPa. The intensity of B_{3g} mode gradually decreasesand this mode disappears at ~10 GPa. The B_{1g} mode, which is hidden in background at ambient pressure, becomes "visible" after 6.8 GPa and increase gradually with further compression. Meanwhile, the Raman mode frequency evolution against pressure was shownin Fig. 6b. A dramatic discontinuous change of slope has been observed at 6.8GPa. When the pressure was releasedto ambient pressure,the initial vibrational modes are recovered, indicating this transition is reversible as well. Because of the Raman is consistent with the ADXRD results in terms of the P_T, we have reasons to assume thata direct link exists and to regard the slope changes as an additional evidence of the pressure-induced structural transition in SnSe.

Recently, SnSehave attracted much attention in the thermoelectric communitydue to the *Cmcm* structure features can induced a strong anharmonicity in bonding and result an intrinsically ultralow lattice thermal conductivity.[64]The mode Grüneisen parameter (γ) is a powerful tool to described the changesin the anharmonic bonding and can bedirectly measured from a single high-pressure experiment. We calculated theγ valuesby the following equation:

$$\gamma = -\frac{d\ln\omega}{d\ln P} = \frac{B_0}{\omega_0}\cdot\frac{d\omega}{dp} \quad (5)$$

where ω_0 and ω are the mode frequencies at ambient pressure and at high pressures, respectively; P and B_0 are pressure andbulk modulus in GPa.The list of all the observedmodes along with their frequencies, assignments and Grüneisen parameter are summarized in Table I.

Conclusions

In summary, we synthesized the high-purity, free-standing and uniform morphology 2D SnSe NSs *via* a plasma assisted DC arc discharge method. The high-pressure behaviors have been investigated by *in situ* synchrotron ADXRD and Raman scattering up to ~30 GPa at room temperature. A second-order isostructural continuous phase transition from orthorhombic structure *Pnma* (62) symmetry to *Cmcm* (63) symmetry has been observed at ~7 GPa, which is much lower than the transition pressure of bulk SnSe. The decreased transition pressure can be attributed to the volumetric expansion with softening of Poisson ratio and shear modulus. In addition, the bulk modulus of *Pnma* phase is consistent with that of bulk SnSe, which is different from the most nanomaterials. We suggested that this abnormal compressibility arise from the unique intrinsic geometry in nanosheet. Meanwhile, we observed a significantly enhanced bulk modulus of *Cmcm* phase compared with theoretical results, which is considered to be caused by the pressure-induced morphology change. We believed that this work not only provided valuable experimental information about the SnSenanosheets, but might also shed some light onto the pressure-induced phase transition behaviors of other IV-VI layered structural compounds at nano-scale.

Acknowledgements

This work was supported financially by the National Natural Science Foundation of China (grant no. 11074089, 51172087, 11304111, 61474009, NSAF. No: U1330115), the Educational commission of Liaoning province of China (L2014448), Specialized Research Fund for the Doctoral Program of Higher Education of China (20110061110011) and the National Basic Research Program of China (grant no. 2011CB808204). Portions of this work were performed at 4W2 beamline, Beijing Synchrotron Radiation Facility (BSRF).

Notes and references

1. J. N. Coleman, M. Lotya, A. O'Neill, S. D. Bergin, P. J. King, U. Khan, K. Young, A. Gaucher, S. De, R. J. Smith, I. V. Shvets, S. K. Arora, G. Stanton, H.-Y. Kim, K. Lee, G. T. Kim, G. S. Duesberg, T. Hallam, J. J. Boland, J. J. Wang, J. F. Donegan, J. C. Grunlan, G. Moriarty, A. Shmeliov, R. J. Nicholls, J. M. Perkins, E. M. Grieveson, K. Theuwissen, D. W. McComb, P. D. Nellist and V. Nicolosi, *Science*, 2011, **331**, 568-571.
2. J. S. Son, J. H. Yu, S. G. Kwon, J. Lee, J. Joo and T. Hyeon, *Adv. Mater.*, 2011, **23**, 3214-3219.
3. X. Huang, S. Tang, X. Mu, Y. Dai, G. Chen, Z. Zhou, F. Ruan, Z. Yang and N. Zheng, *Nat. Nanotechnol.*, 2011, **6**, 28-32.
4. T. Yu, B. Lim and Y. Xia, *Angew. Chem.Int. Edit.*, 2010, **49**, 4484-4487.
5. C. Schliehe, B. H. Juarez, M. Pelletier, S. Jander, D. Greshnykh, M. Nagel, A. Meyer, S. Foerster, A. Kornowski, C. Klinke and H. Weller, *Science*, 2010, **329**, 550-553.
6. A. K. Geim and K. S. Novoselov, N*at. Mater.*, 2007, **6**, 183-191.
7. K. Y. Lee, J. R. Lim, H. Rho, Y. J. Choi, K. J. Choi and J. G. Park, *Appl. Phys. Lett.*, 2007, **91**, 201901.
8. T. Sasaki and M. Watanabe, J.Phys. Chem. B, 1997, 101, 10159-10161.
9. K. Fukuda, K. Akatsuka, Y. Ebina, R. Ma, K. Takada, I. Nakai and T. Sasaki, *ACS Nano*, 2008, **2**, 1689-1695.
10. M. Osada and T. Sasaki, *J. Mater. Chem.*, 2009, **19**, 2503-2511.
11. N. Sakai, Y. Ebina, K. Takada and T. Sasaki, *J. Am. Chem. Soc.*, 2004, 126, 5851-5858.
12. M. Osada, Y. Ebina, K. Fukuda, K. Ono, K. Takada, K. Yamaura, E. Takayama-Muromachi and T. Sasaki, *Phys. Rev. B*, 2006, **73**, 153301.
13. J. Zhang, J. M. Soon, K. P. Loh, J. Yin, J. Ding, M. B. Sullivian and P. Wu, *Nano. Lett.*, 2007, 7, 2370-2376.. Zhang, J. M. Soon, K. P. Loh, J. Yin, J. Ding, M. B. Sullivian and P. Wu, Nano Letters, 2007, 7, 2370-2376.
14. E. Coronado, C. Martí-Gastaldo, E. Navarro-Moratalla, A. Ribera, S. J. Blundell and P. J. Baker, *Nat. Chem.*, 2010, 2, 1031-1036.
15. M. X. Wang, C. H. Liu, J. P. Xu, F. Yang, L. Miao, M. Y. Yao, C. L. Gao, C. Y. Shen, X. C. Ma, X. Chen, Z. A. Xu, Y. Liu, S. C. Zhang, D. Qian, J. F. Jia and Q. K. Xue, *Science*, 2012, **336**, 52-55.
16. P. D. Antunez, J. J. Buckley and R. L. Brutchey, *Nanoscale*, 2011, **3**, 2399-2411.
17. S. Liu, X. Y. Guo, M. R. Li, W. H. Zhang, X. Y. Liu and C. Li, *Angew. Chem.Int. Edit.*, 2011, **50**, 12050-12053.
18. G. Valiukonis, D. A. Guseinova, G. Keivaitb and A. Sileika, *Phys.Status. Solidi.B*, 1986, **135**, 299-307.
19. X. Liu, Y. Li, B. Zhou, X. L. Wang, A. N. Cartwright and M. T. Swihart, *Chem. Mater.*, 2014, **26**, 3515-3521.
20. X. F. Wang, B. Liu, Q. Y. Xiang, Q. F. Wang, X. J. Hou, D. Chen and G. Z. Shen, *Chemsuschem*, 2014, **7**, 308-313.
21. M. A. Franzman, C. W. Schlenker, M. E. Thompson and R. L. Brutchey, *J. Am. Chem. Soc.*, 2010, **132**, 4060-4061.
22. W. J. Baumgardner, J. J. Choi, Y. F. Lim and T. Hanrath, *J. Am. Chem. Soc.*, 2010, **132**, 9519-9521.
23. G. Shen, D. Chen, X. Jiang, K. Tang, Y. Liu and Y. Qian, *Chem. Lett.*, 2003, **32**, 426-427.
24. D. D. Vaughn, S. I. In and R. E. Schaak, *Acs Nano*, 2011, **5**, 8852-8860.
25. L. Li, Z. Chen, Y. Hu, X. W. Wang, T. Zhang, W. Chen and Q. B. Wang, *J. Am. Chem. Soc.*, 2013, **135**, 1213-1216.
26. P. Kevin, S. N. Malik, M. A. Malik and P. O'Brien, *Chem. Commun.*, 2014, **50**, 14328-14330.

27. N. D. Boscher, C. J. Carmalt, R. G. Palgrave and I. P. Parkin, *Thin. Solid. Films.*, 2008, **516**, 4750-4757.
28. X. H. Ma, K. H. Cho and Y. M. Sung, *CrystEngComm.*, 2014, **16**, 5080-5086.
29. T. Chattopadhyay, A. Werner, H. G. Von Schnering and J. Pannetier, *Rev. Phys. Appl.*, 1984, **19**, 807-813.
30. M. J. Peters and L. E. McNeil, *Phys. Rev. B*, 1990, **41**, 5893-5897.
31. M. Parenteau and C. Carlone, *Phys. Rev. B*, 1990, **41**, 5227-5234.
32. A. Agarwal, S. H. Chaki, S. G. Patel and D. Lakshminarayana, *J. Mater. Sci-Mater. El.*, 1994, **5**, 287-290.
33. I. Loa, R. J. Husband, R. A. Downie, S. R. Popuri and J. W. G. Bos, *J. Phys. Condens.Mat.*, 2015, **27**, 072202-072202.
34. M. Durandurdu, *Phys. Rev. B*, 2005, **72**, 144106.
35. F. M. Gashimzade, D. A. Guseinova, Z. A. Jahangirli, B. G. Mekhtiev and G. S. Orudzhev, *Phys. Solid. State.*, 2014, **56**, 761-764.
36. S. Alptekin and M. Durandurdu, *Solid. State. Commun.*, 2010, **150**, 870-874.
37. S. Alptekin, *J. Mol. Model.*, 2011, **17**, 2989-2994.
38. W. W. Lei, D. Liu, Y. M. Ma, X. Chen, F. B. Tian, P. W. Zhu, X. H. Chen, Q. L. Cui and G. T. Zou, *Angew. Chem.Int. Edit.*, 2010, **49**, 173-176.
39. H. K. Mao, J. Xu and P. M. Bell, *J. Geophys. Res. Solid. Earth.*, 1986, **91**, 4673-4676.
40. A. Hagfeldt and M. Graetzel, *Chem. Rev.*, 1995, **95**, 49-68.
41. V. E. Drozd, I. O. Nikiforova, V. B. Bogevolnov, A. M. Yafyasov, E. O. Filatova and D. Papazoglou, *J. Phys. DAppl. Phys.*, 2009, **42**, 125306.
42. B. Pejova and A. Tanuševski, *J. Phys. Chem.C*, 2008, **112**, 3525-3537.
43. D. Chun, R. M. Walser, R. W. Bené and T. H. Courtney, *Appl. Phys. Lett.*, 1974, **24**, 479-481.
44. H. G. Von. Schnering and H. Wiedemeier, *Z. Kristallogr.*, 1981, **156**, 143-150.
45. F. Birch, *Phys. Rev.*, 1947, **71**, 809-824.
46. I. Efthimiopoulos, J. Kemichick, X. Zhou, S. V. Khare, D. Ikuta and Y. Wang, *J. Phys. Chem. A*, 2014, **118**, 1713-1720.
47. F. J. Manjón, R. Vilaplana, O. Gomis, E. Pérez-González, D. Santamaría-Pérez, V. Marín-Borrás, A. Segura, J. González, P. Rodríguez-Hernández, A. Muñoz, C. Drasar, V. Kucek and V. Muñoz-Sanjosé, *Phys.Status. Solidi.B*, 2013, **250**, 669-676.
48. Z. W. Wang, Y. Zhao, D. Schiferl, J. Qian, R. T. Downs, H. K. Mao and T. Sekine, *J. Phys. Chem.B*, 2003, **107**, 14151-14153.
49. S. H. Tolbert and A. P. Alivisatos, *Science*, 1994, **265**, 373-376.
50. P. Villain, P. Goudeau, P. O. Renault and K. F. Badawi, *Appl. Phys. Lett.*, 2002, **81**, 4365-4367.
51. T. D. Shen, C. C. Koch, T. Y. Tsui and G. M. Pharr, *J. Mater. Res.*, 1995, **10**, 2892-2896.
52. Y. Zhou, U. Erb, K. T. Aust and G. Palumbo, *Scripta. Mater.*, 2003, **48**, 825-830.
53. J. E. Spanier, R. D. Robinson, F. Zhang, S. W. Chan and I. P. Herman, *Phys. Rev. B*, 2001, **64**, 245407.
54. Z. W. Wang, S. K. Saxena, V. Pischedda, H. P. Liermann and C. S. Zha, *Phys. Rev. B*, 2001, **64**, 012102.
55. Z. W. Wang, S. K. Saxena, V. Pischedda, H. P. Liermann and C. S. Zha, *J. Phys. Condens.Mat.*, 2001, **13**, 8317.
56. J. Z. Jiang, J. S. Olsen, L. Gerward and S. Morup, *Europhys. Lett.*, 1999, **45**, 275-275.
57. J. N. Wickham, A. B. Herhold and A. P. Alivisatos, *Phys. Rev. Lett.*, 2000, **84**, 923-926.
58. Z. W. Wang and Q. Guo, *J. Phys. Chem.C*, 2009, **113**, 4286-4295.
59. S. H. Tolbert and A. P. Alivisatos, *Annu. Rev. Phys. Chem.*, 1995, **46**, 595-625.
60. Z. W. Wang, K. Finkelstein, C. Ma and Z. L. Wang, *Appl. Phys. Lett.*, 2007, **90**, 113115.
61. Z. W. Wang, X. D. Wen, R. Hoffmann, J. S. Son, R. Li, C.C. Fang, D.M. Smilgies and T. Hyeon, *P. Natl. Acad. Sci.*, 2010, **107**, 17119-17124.
62. G. Xiao, K. Wang, L. Zhu, X. Tan, Y. Qiao, K. Yang, Y. Ma, B. Liu, W. Zheng and B. Zou, *J. Phys. Chem.C*, 2015, **119**, 3843-3848.
63. M. Ludemann, O. D. Gordan, D. R. T. Zahn, M. Beekman, R. Atkins and D. C. Johnson, *Langmuir*, 2014, **30**, 8209-8214.
64. L. D. Zhao, S. H. Lo, Y. S. Zhang, H. Sun, G. J. Tan, C. Uher, C. Wolverton, V. P. Dravid and M. G. Kanatzidis, *Nature*, 2014, **508**, 373-377.

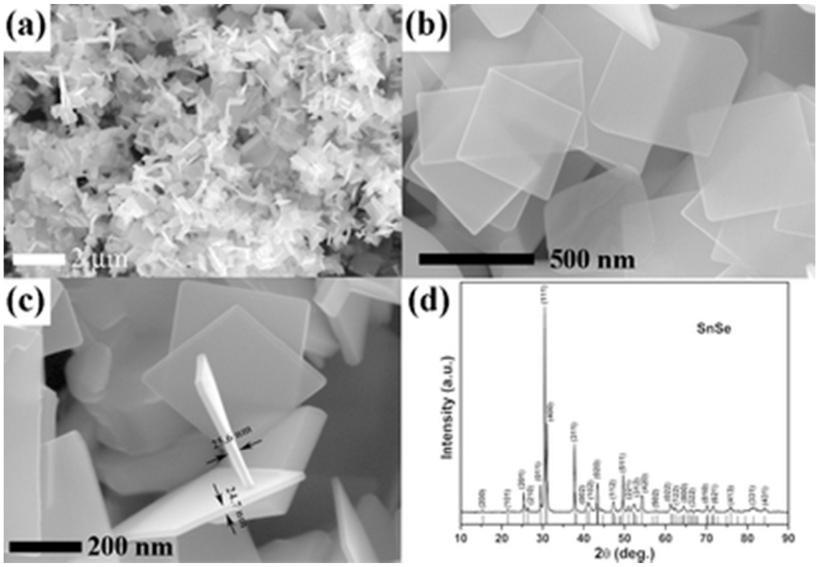

Fig. 1 Low- (a) and High- ((b) and (c)) magnification SEM images and XRD patterns (d) of SnSe NSs.
34x23mm (300 x 300 DPI)

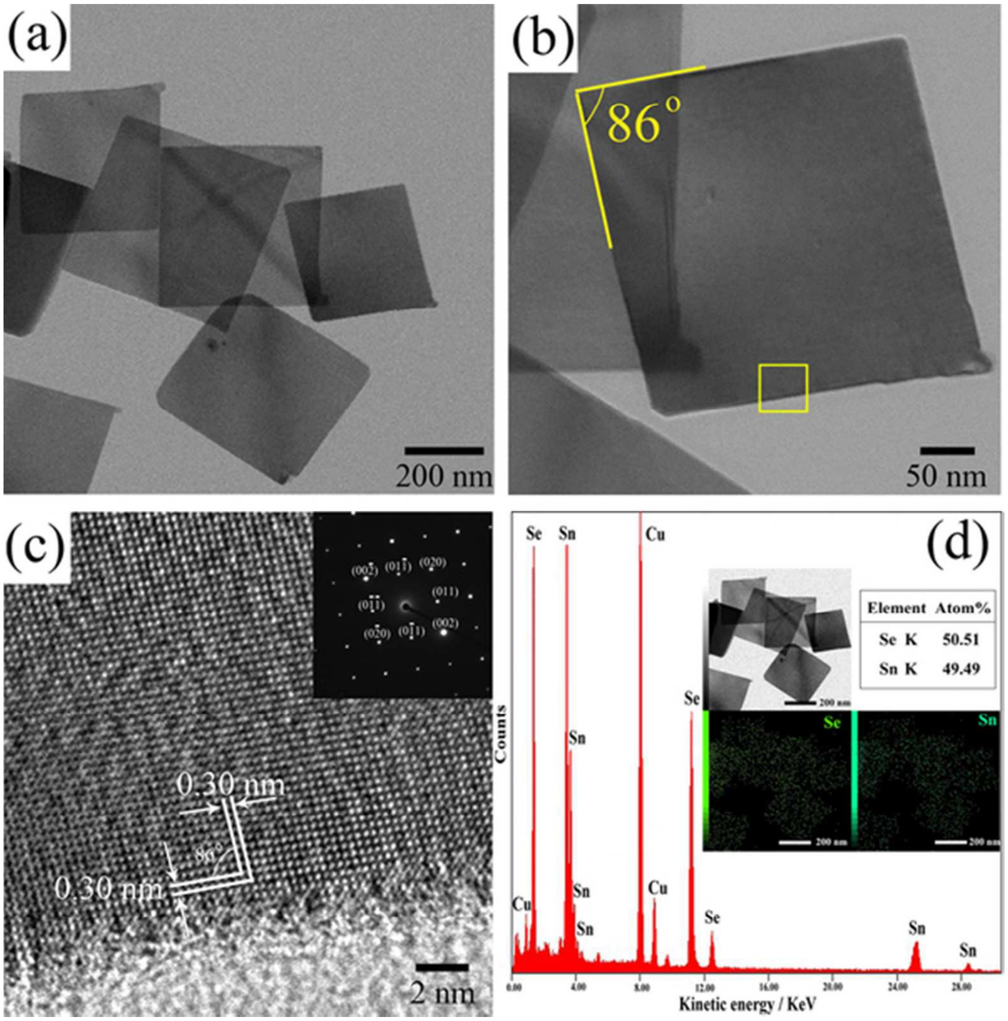

Element	Atom%
Se K	50.51
Sn K	49.49

Fig. 2 TEM, HRTEM images and SAED pattern (a, b, c and inset) of SnSe NSs. EDS, elemental distribution and atom ratio (d) of SnSe NSs.
50x51mm (300 x 300 DPI)

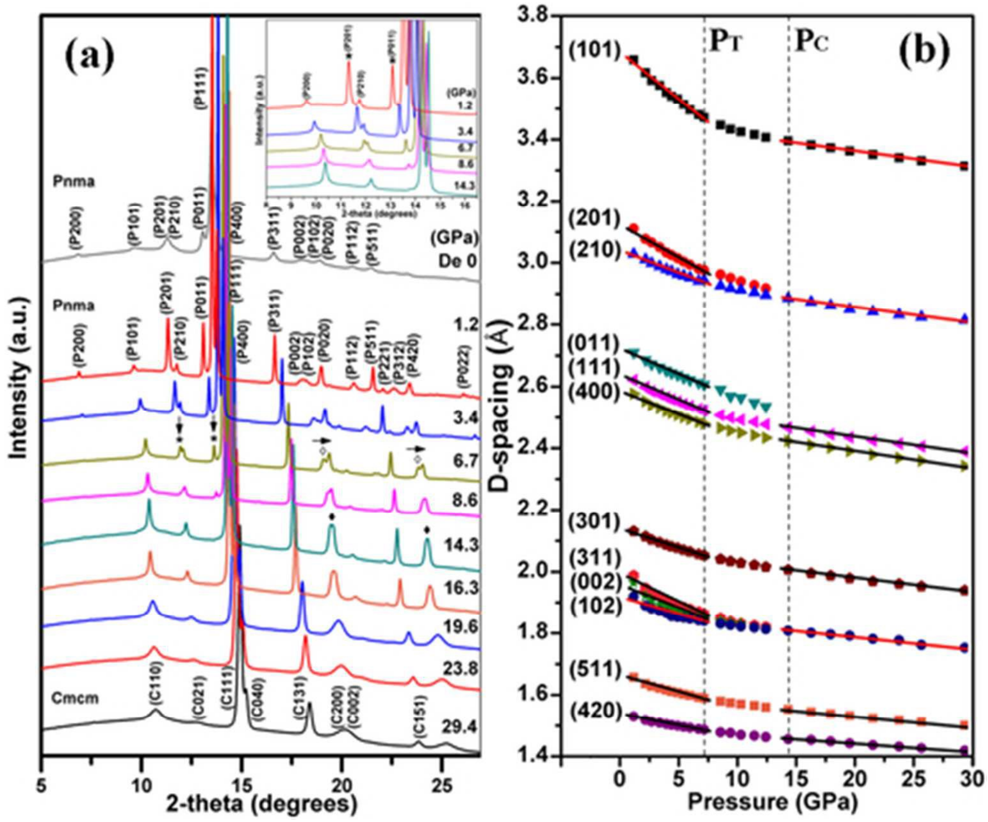

Fig.3 Representative ADXRD patterns of SnSe NSs at selected pressures. The down and right arrows (↓ and →) illustrate the evolution of specified peaks (marked with asterisk (*) and hollow diamond (◇)). The solid diamonds (◆) represent that these specified peaks completely merge with their adjacent peaks at 14.3 GPa. The top pattern is collected after releasing the pressure. The inset illustrates the pressure-induced reduction in intensity and disappearance of the (201) and (011) diffraction peaks. (a) *d*-spacing as a function of pressure at room temperature. The Vertical dotted lines represent the pressure of phase transition started (P_T = 6.7 GPa) and completed (P_C = 14.3 GPa). (b)
41x34mm (300 x 300 DPI)

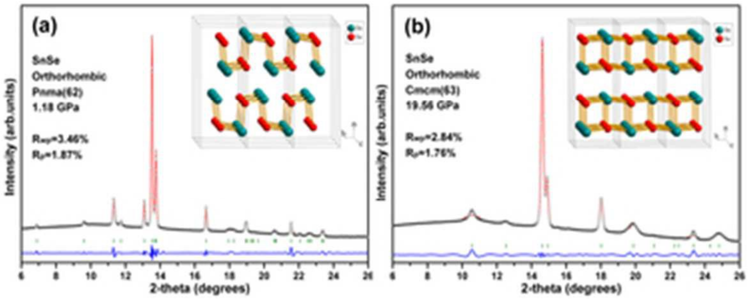

Fig. 4 Full profile Rietveld refinement of the powder ADXRD patterns of SnSe obtained at 1.18 GPa (a) and 19.56 GPa (b), respectively. The blue line denotes the difference between the observed (red) and the simulated (black) profiles. Bars are marked at the positions of diffraction peaks. The insets represent corresponding crystal structural representations. TEM, HRTEM images and SAED pattern (a, b, c and inset) of SnSe NSs. EDS, elemental distribution image and atom ratio (d) of SnSe NSs.
31x12mm (300 x 300 DPI)

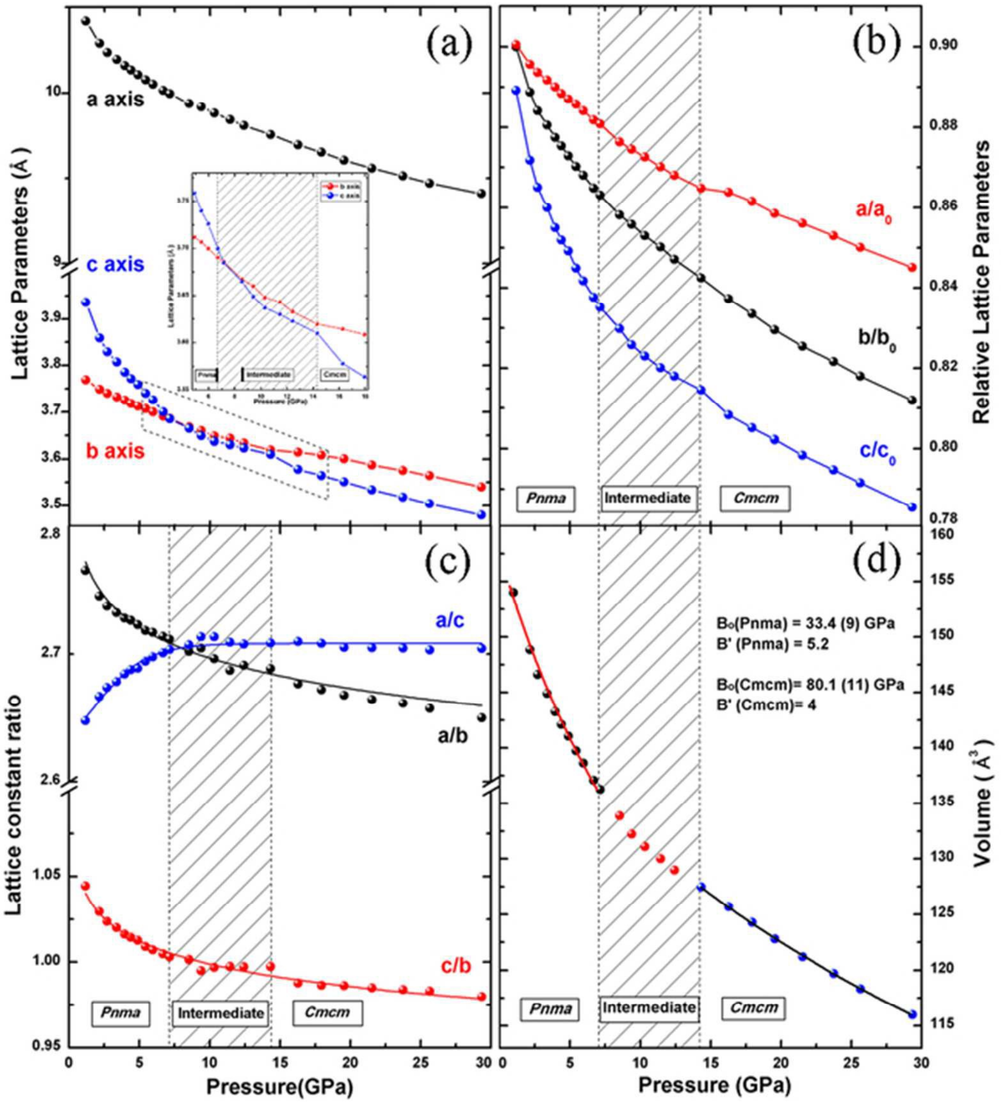

Fig. 5 Lattice parameters (a), Relative lattice parameters (b) and Axial Ratios (*a*/*c*, *a*/*b* and *c*/*b*) (c) as a function of pressure. The spheres denote the experimental data and lines are guides to the eye. Pressure-volume relation of SnSe NSs (d). The results are fitted to Birch−Murnaghan equation. The dashed areas represent the phase transition pressure range.
54x60mm (300 x 300 DPI)

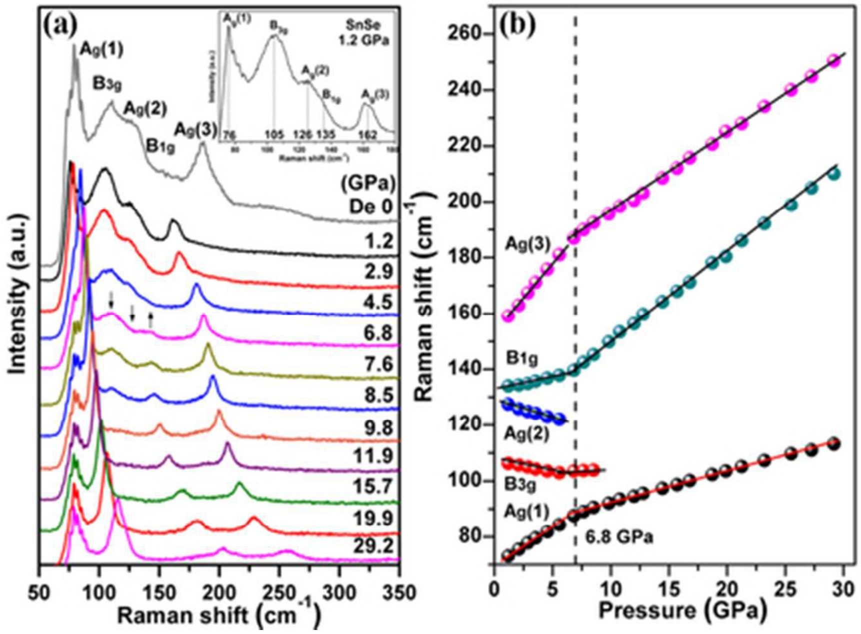

Fig. 6 Selected Raman spectra of SnSe at high-pressures (a) and at 1.2 GPa (inset). The up and down arrows represent the enhanced and weakened intensities of vibrational modes, respectively. The top pattern is collected after releasing the pressure. Pressure dependence of Raman frequency shifts in SnSe (b). Vertical dotted lines indicate phase transition pressure.
36x26mm (300 x 300 DPI)